Geochemistry Geophysics Geosystems G3

Article
Volume 13, Number 6
23 June 2012
Q06016, doi:10.1029/2012GC004164
ISSN: 1525-2027

Published by AGU and the Geochemical Society

Unraveling the apparent magnitude threshold of remote earthquake triggering using full wavefield surface wave simulation

Tom Parsons and J. Ole Kaven
U.S. Geological Survey, MS-999, 345 Middlefield Road, Menlo Park, California 94025, USA (tparsons@usgs.gov)

Aaron A. Velasco and Hector Gonzalez-Huizar
Department of Geological Sciences, University of Texas at El Paso, El Paso, Texas 79968, USA

[1] Empirical studies with earthquake catalogs suggest that large events ($M > 5$) are rarely triggered in significant numbers by passing surface waves at remote distances from main shocks. Triggered, small ($M < 5$) earthquakes are routinely associated with the passage of surface waves from large ($M > 7$) main shocks. Since large earthquakes involve larger rupture areas, we study the spatial and temporal characteristics of dynamic stress change for clues. Using a 3D finite element method, we model the complete wavefield from the 2002 $M = 7.9$ Denali earthquake recorded near the Wasatch Front in Utah, where details about triggered seismicity are known. In particular, we load our model with a displacement seismogram to acquire a time series of the stress change tensor and model failure of a representative normal fault based on these stress changes. We note that the stress-change regime varies rapidly between favoring strike-slip, thrust, and normal faulting, with durations lasting ~1–4 s. We find that these stress regimes usually affect only some fraction of a fault surface at any given time. Stress amplitudes also vary, meaning that ideal conditions for triggering are short-lived and spatially limited. Stress conditions can also rapidly reverse to regimes that inhibit slip. Given these stressing conditions, we conclude that it may be difficult for a larger rupture area to experience the temporally and spatially coherent stress change necessary to develop into a large magnitude earthquake.

Components: 6200 words, 13 figures.

Keywords: dynamic triggering; earthquake triggering; finite element modeling; surface waves.

Index Terms: 7223 Seismology: Earthquake interaction, forecasting, and prediction (1217, 1242, 4315); 7230 Seismology: Seismicity and tectonics (1207, 1217, 1240, 1242); 7255 Seismology: Surface waves and free oscillations.

Received 26 March 2012; **Revised** 18 May 2012; **Accepted** 18 May 2012; **Published** 23 June 2012.

Parsons, T., J. O. Kaven, A. A. Velasco, and H. Gonzalez-Huizar (2012), Unraveling the apparent magnitude threshold of remote earthquake triggering using full wavefield surface wave simulation, *Geochem. Geophys. Geosyst.*, *13*, Q06016, doi:10.1029/2012GC004164.

1. Introduction

[2] Earthquakes are commonly triggered by seismic waves from a large earthquake ($M > 7$) originating thousands of km away [*Hill et al.*, 1993; *Brodsky et al.*, 2000; *Kilb et al.*, 2000; *Gomberg et al.*, 2001, 2004; *West et al.*, 2005]. Large earthquakes produce surface waves that travel global distances within a crustal waveguide, and can temporarily distort and stress fault planes that lie in their paths. Observations of direct triggering by seismic waves seem to involve smaller ($M < 5$) earthquakes [e.g., *Hill and Prejean*, 2007; *Velasco et al.*, 2008], and it has been difficult to observe a significant pattern of larger, more dangerous events being advanced by dynamic stressing [*Huc and Main*, 2003; *Parsons and Velasco*, 2011]. It is unclear why there appears to be a magnitude dependence associated with dynamic triggering.

[3] A difficulty posed by dynamic earthquake triggering phenomena is that the physical process is not well understood. A number of models and ideas for how fault failure might be prompted through transient deformation by seismic waves have been proposed, including changes in the rate/state friction setting within faults [e.g., *Gomberg et al.*, 1997; *Scholz*, 1998; *Gomberg et al.*, 1998; *Belardinelli et al.*, 2003; *Parsons*, 2005], induced fluid pressure changes [e.g., *Hill et al.*, 1993; *Sturtevant et al.*, 1996; *Brodsky et al.*, 2003; *Brodsky and Prejean*, 2005], as well as direct transient Coulomb stressing [e.g., *Kilb et al.*, 2002; *Hill*, 2008]. As all of these processes are generalized to earthquake nucleation, they likely play roles in remote earthquake triggering in varying proportions.

[4] Other than in deep drilling experiments [e.g., *Oye and Ellsworth*, 2007], we cannot directly sample earthquake nucleation sites. However, there are empirical data that enable an indirect, numerical view of the temporal and spatial patterns of dynamic stressing. Here we use observed transient strains from the 2002 $M = 7.9$ Denali earthquake in Utah (Figure 1), to model the time series of dynamic stressing. We choose this source earthquake and triggering setting because the Wasatch zone in eastern Utah was the site of increased seismicity immediately during and after the passage of surface waves from the Denali main shock, and was studied in detail by *Pankow et al.* [2004]. Many sites in western North America were also affected [*Gomberg et al.*, 2004] (Figures 2 and 3).

[5] Examination of the raw global earthquake catalog for 24-h periods before and after the 2002 $M = 7.9$ Denali event shows pockets of apparently triggered seismicity in the western U.S. (Figure 3). Issues of detection and completeness with the raw catalog data [e.g., *Kagan*, 2004; *Iwata*, 2008] could mask a more widespread micro-seismic response. The post-Denali signal typifies global compilations of dynamic triggering observations, showing a significant near-source rate increase at all magnitudes, no discernable global effect on the rate of larger ($M > 5$) seismicity [e.g., *Huc and Main*, 2003], while provoking clear micro-earthquake rate changes detectable by regional networks (Figure 3). In this paper we seek to understand whether there are special stressing conditions that apply to remote earthquake triggering that are absent in the near-field region.

2. Dynamic Stressing: Modeling Strategy

[6] Previous studies of remote dynamic triggering have examined stressing from individual surface wave components (Love and Rayleigh waves), and have correlated triggered seismicity with them [e.g., *Hill*, 2008; *Gonzalez-Huizar and Velasco*, 2011]. In the near field, *Kilb et al.* [2002] and *Kilb* [2003] modeled displacement seismograms to get peak dynamic Coulomb stress changes. Here we are particularly interested in the spatial and temporal extent of dynamic stress changes resolved on triggered faults, since we want to understand why there is an apparent upper magnitude threshold on dynamically triggered events. As such, we choose to model the complete surface wave train, which mixes Love and Rayleigh wave components and their coda (Figure 1) as it passes over faults, so we can track the complete stress-change tensor as it evolves with time. To accomplish this, we use a commercial finite element modeling approach (ANSYS®) to simulate the time series of stress changes associated with passing seismic waves based on measured 3D displacements. After we calculate the dynamic stress change tensor, we examine its effects at a point, and then we model failure of an example fault surface.

[7] We create a finite element model that is a beam 125 km long, 25 km wide, and 10 km deep, aimed in the propagation direction (N43.1°W) between the Denali earthquake epicenter and the recording site (Figure 4). The finite element model is discretized into 1.6 km cubic elements that are given

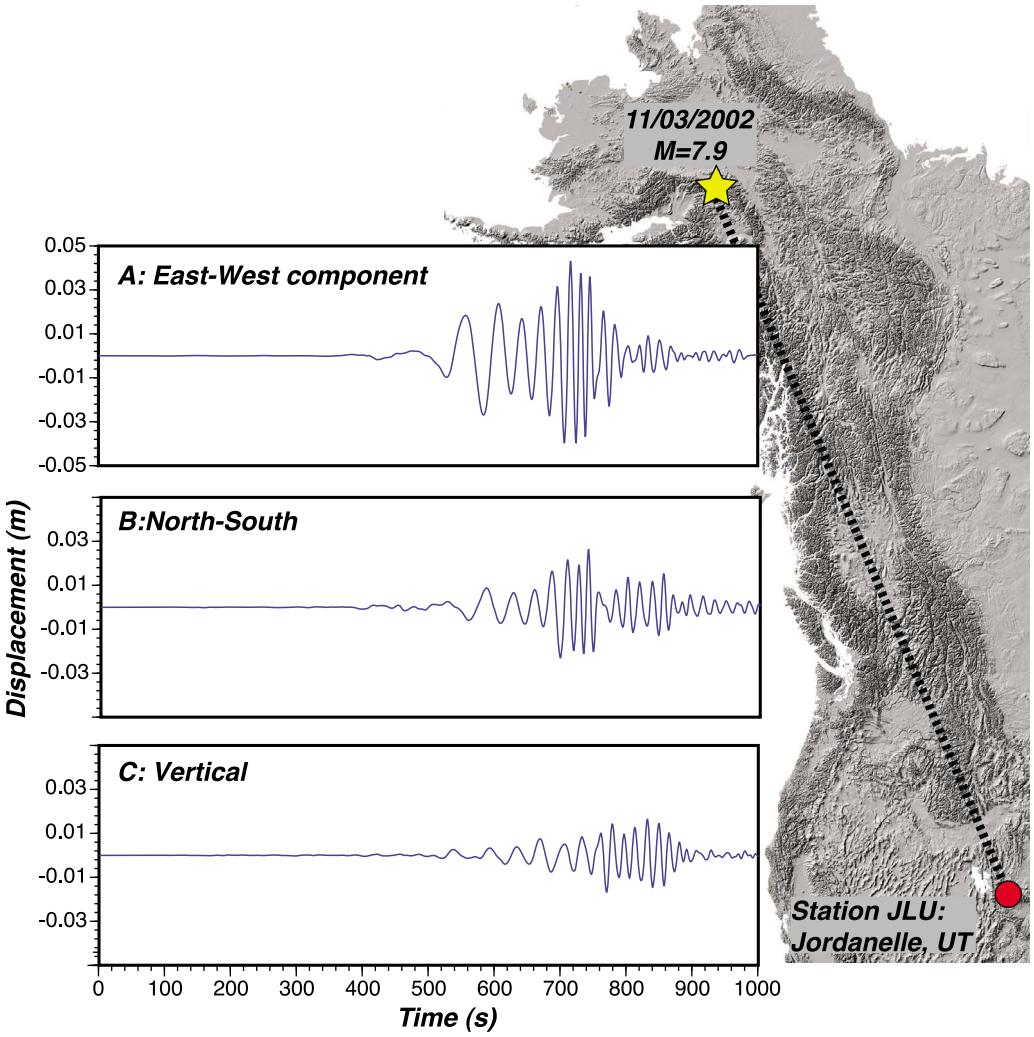

Figure 1. Seismograms showing 3D displacements that occurred at Jordanelle, UT as seismic waves from the 2002 $M = 7.9$ Denali earthquake passed through the region. Traces are shown with a bandpass filter of 10 to 0.05 Hz, and the sample interval of 0.4 s that is used in numerical stress modeling.

material properties representing granite, with a Young's modulus of $E = 80$ GPa [*Birch*, 1966].

[8] Model loading is taken from a 1000-s-long displacement seismogram recorded at station JLU (Jordanelle Reservoir, Utah; 40.6020°N, 111.4500°W). The highest amplitude signals at this range are surface waves (Figure 1). We calculate depth kernels for the surface waves and translate surface displacements to displacements at depth within the elastic model. To make the numerical problem solvable in a reasonable time, we subsampled the seismograms to 0.4 s intervals, causing the shortest meaningful periods we capture to be 5 s. Time- and space-dependent loads are then applied at every point throughout the model sequentially (Figure 5), as defined by the displacement seismogram (Figure 6). Each point in the model experiences all the measured 3D displacements in order, as the waves propagate through the model at 4 km/s.

[9] A key issue in the modeling is to establish proper boundary conditions. If the model were to have any fixed edges, large stresses would result at transitions between strained and fixed parts of the model. Our solution is to model a sufficiently long section of crust (125 km) aimed along the azimuth between the seismograph and Denali earthquake epicenter (N43.1°W) such that a significant duration of the waveform can be occurring across the model simultaneously (Figures 4 and 5). In this way, all imposed displacements and resulting stresses are expressed relative to other deforming parts of the crust (Figure 5), rather than to fixed boundaries.

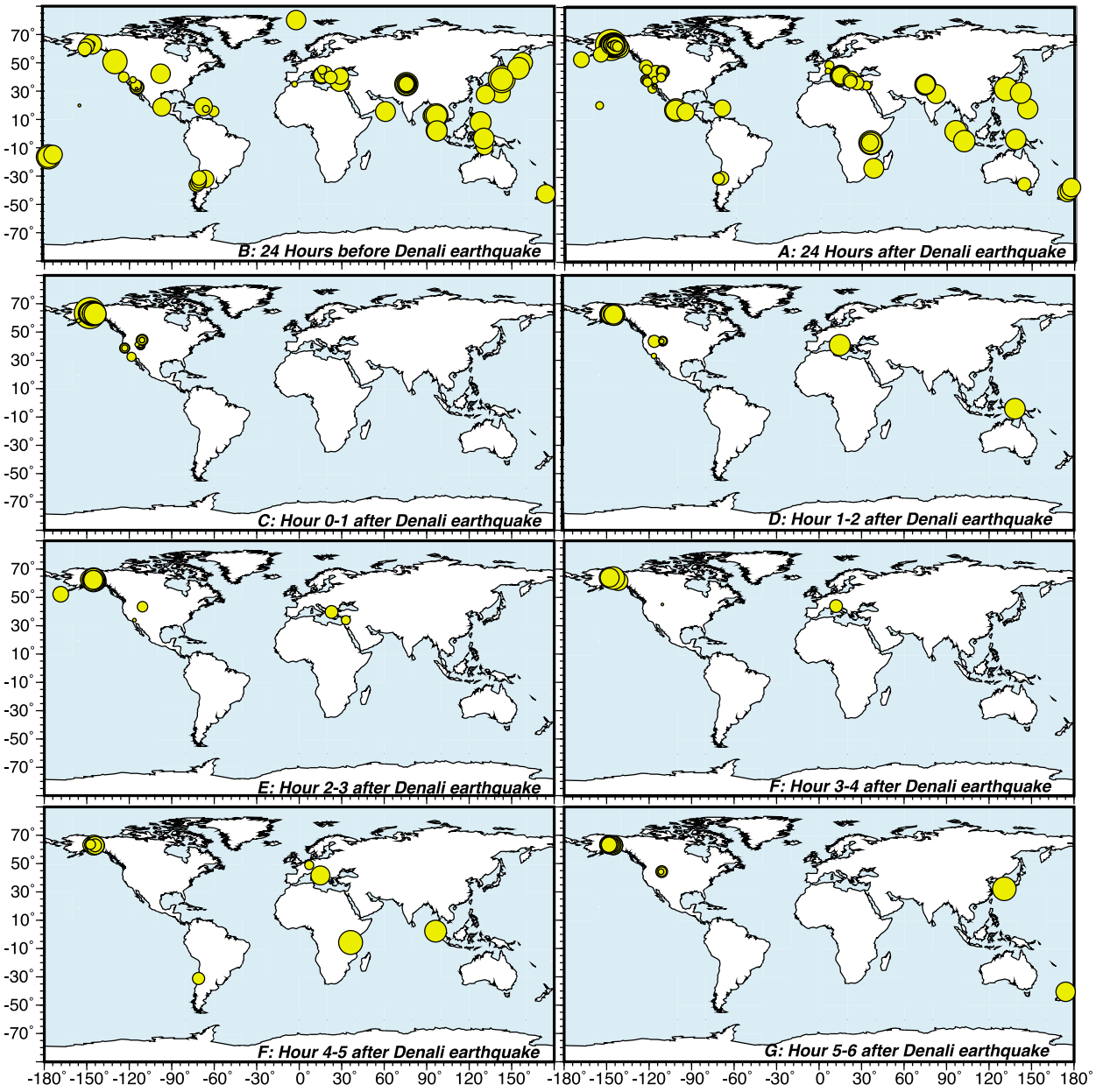

Figure 2. Maps of seismicity (source: Advanced National Seismic System (ANSS)) during 24 h (a) before 2002 M = 7.9 Denali earthquake, (b) 24 h after the event, and (c–g) over hourly increments after. The most obvious dynamic triggering occurs in the western United States along an azimuthal path associated with the maximum measured displacements [*Gomberg et al.*, 2004; *Pankow et al.*, 2004]. A more global effect on earthquake rates is less evident on the maps, though detection thresholds are strongly region-dependent.

[10] The model is only quasi-3D because we extrapolate displacements measured at a single point under the assumption that on the 125 km × 25 km scale of our model, we would not expect significant spatial variation in the long-period surface wave character. Thus, any wave propagation variation from local crustal structure is not simulated. Finally, since we assume there is minimal curvature in the seismic wavefront on our model scale, it is advanced uniformly on a vertical 25-km-wide by 10-km-deep plane along the model. Thus, spatial variations in stressing that we calculate for any given fault plane are primarily related to the geometrical setting (strike and dip) of that plane relative to the propagating wavefront.

[11] Our modeling task is computationally intensive because the 1000-s-long seismogram requires 2500 separate sets of 3D displacements to fully define it.

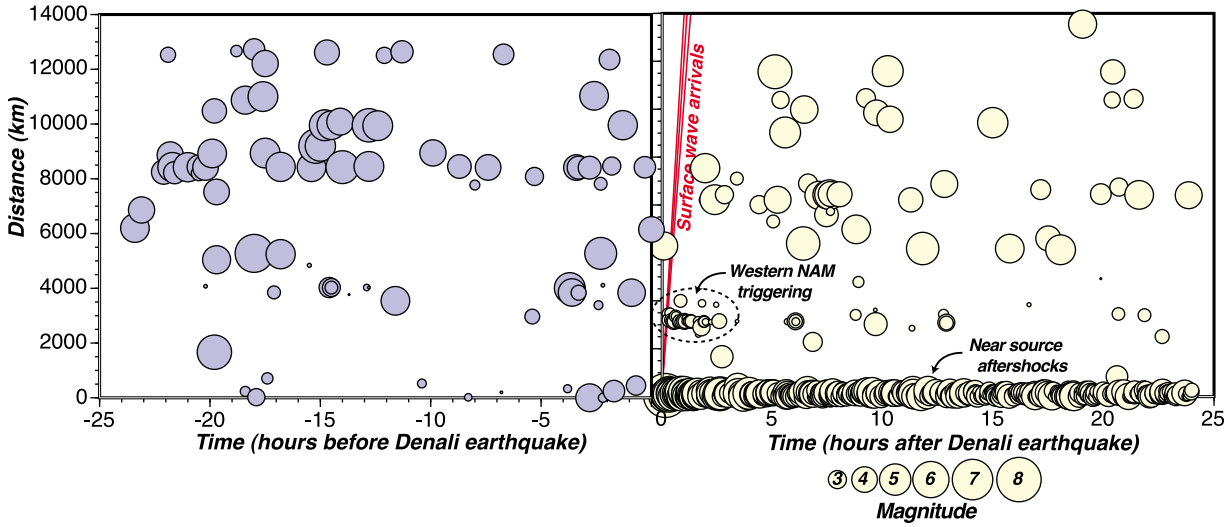

Figure 3. Time-distance plots of the 24-h periods before and after the 2002 $M = 7.9$ Denali earthquake. Global distance ranges from the Denali epicenter are calculated with the inverse method of *Vincenty* [1975] using the NAD83 ellipsoid. Seismicity data are from the ANSS catalogs and have strongly varying location-dependent detection levels. There is thus no minimum magnitude completeness level implied. Detection could be further impacted by the occurrence of the Denali event itself [e.g., *Kagan*, 2004; *Iwata*, 2008]. However, the figure does provide an indication of background rates prior to the Denali event, and shows clear near-source, and western North American seismicity rate increases.

These displacement sets are repeated 79 times as the waves are advanced across the model at 4 km/s. The model has a total of 10,225 nodes, each of which is given a north, east, and vertical displacement at every step (Figure 6). Therefore, propagating the entire 3D seismogram through the model requires 6,058,312,500 separate instructions.

[12] Therefore we did not attempt a fully dynamic solution with inertial terms, but instead approximate

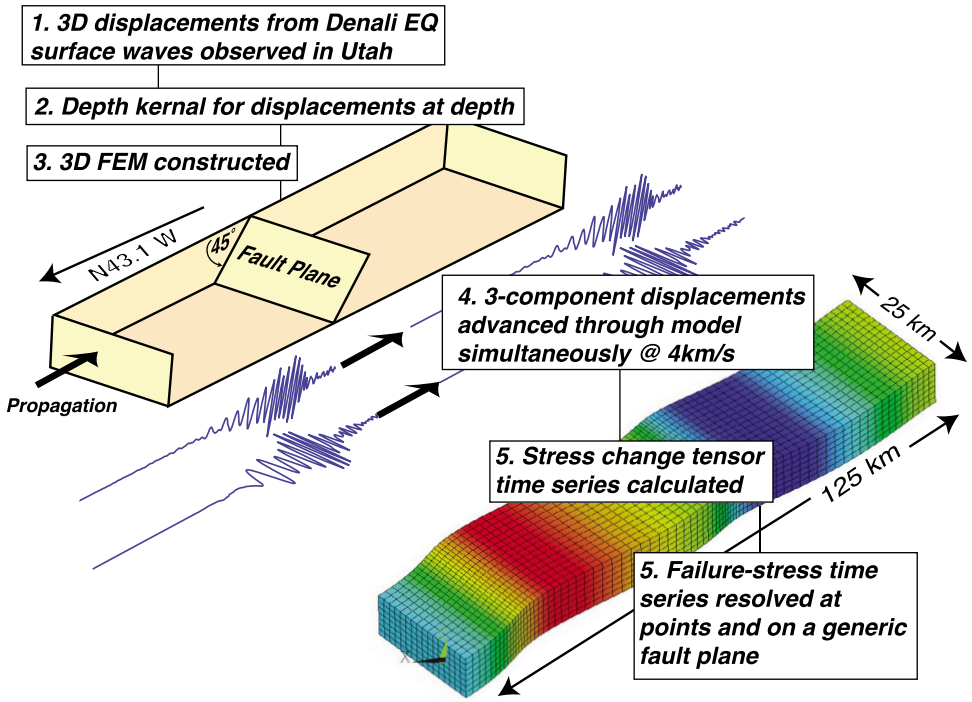

Figure 4. Flowchart of the methods applied to calculate failure stresses resulting from the Denali earthquake at a remote site in Utah. 3D finite element model displacements are exaggerated by a factor of 105 for visualization.

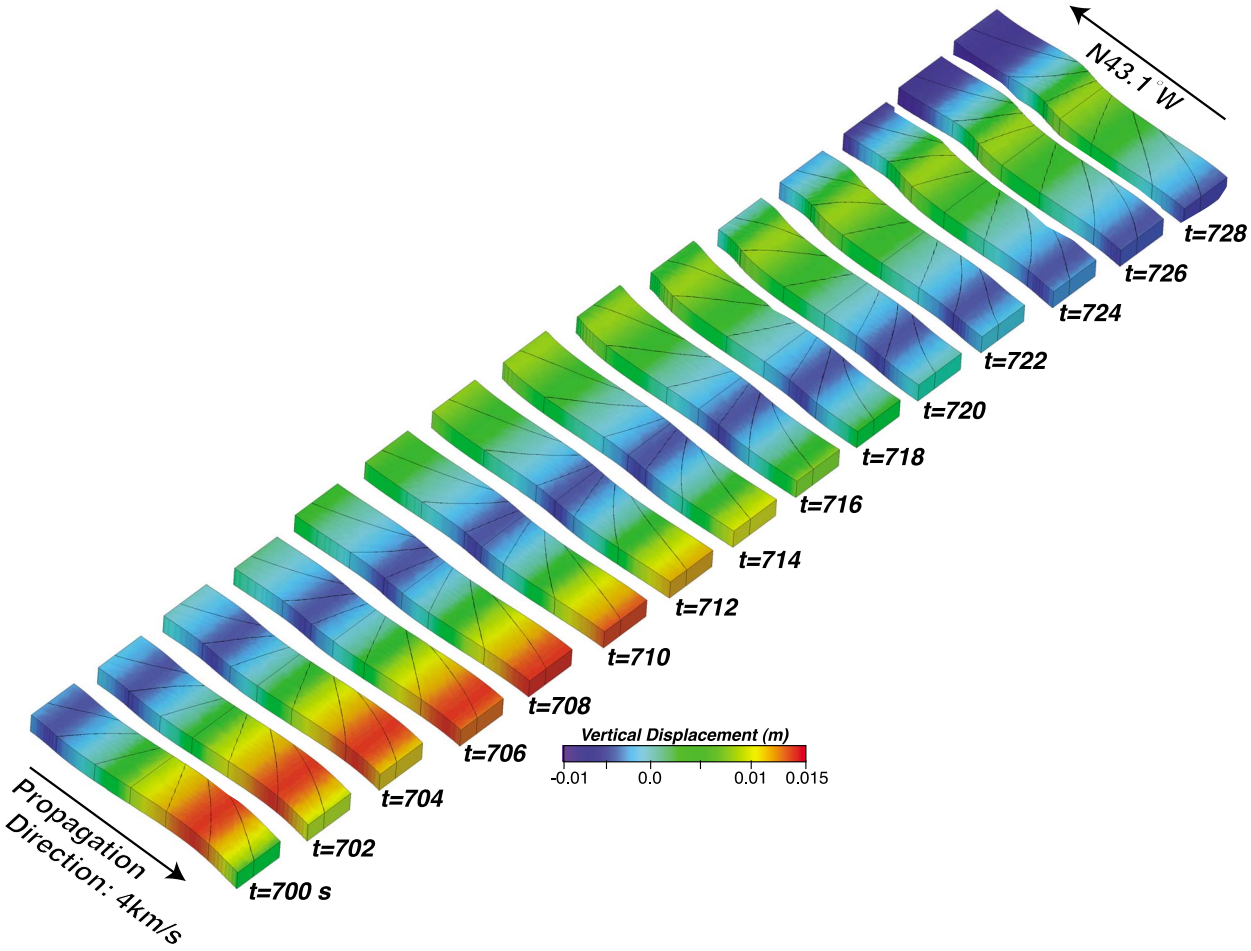

Figure 5. Evolution of displacements versus time as one set of peaks and troughs pass through the model. Calculated stress and strain tensors at any given point are interdependent, but do not result from any fixed boundary conditions.

with a time-varying static model. Time and space varying stress change tensors calculated at model nodes are not affected by this simplification because they are applied to an elastic solid. Inertial effects are more important when studying the response of a time-dependent frictional surface [e.g., *Roy and Marone*, 1996; *Belardinelli et al.*, 2003; *Capozza et al.*, 2009] because they could continue to influence nucleation beyond the time the initial stress change is imposed. We use a time-independent Coulomb failure criterion in our fault-based studies presented in later sections, thus inertial effects are not crucial to our results.

3. Modeled Time Series of Stress Change From Surface Waves

[13] The key result we obtain from numerical simulation is a time varying stress tensor that can be used to calculate expected shear tractions and normal stresses acting on a representative fault plane of the sort found in the extending Basin and Range crust of Utah, where dynamic earthquake triggering was observed [*Pankow et al.*, 2004]. We begin by considering the simplest concept of dynamic triggering, direct Coulomb stress changes at a point. While it has been noted that dynamic triggering can occur preferentially in volcanic centers [e.g., *Brodsky and Prejean*, 2005], *Pankow et al.* [2004] found that post-Denali activity in Utah was not correlated with locations of Quaternary volcanic vents. This suggests that the Utah triggered seismicity represents many tectonic events, and that standard Coulomb failure theory may be applicable.

[14] To calculate Coulomb stress changes at a point, we take shear stress changes to be positive in any direction, which is a maximum interpretation because failure stress is inversely proportional to the angle between target fault rake and imposed

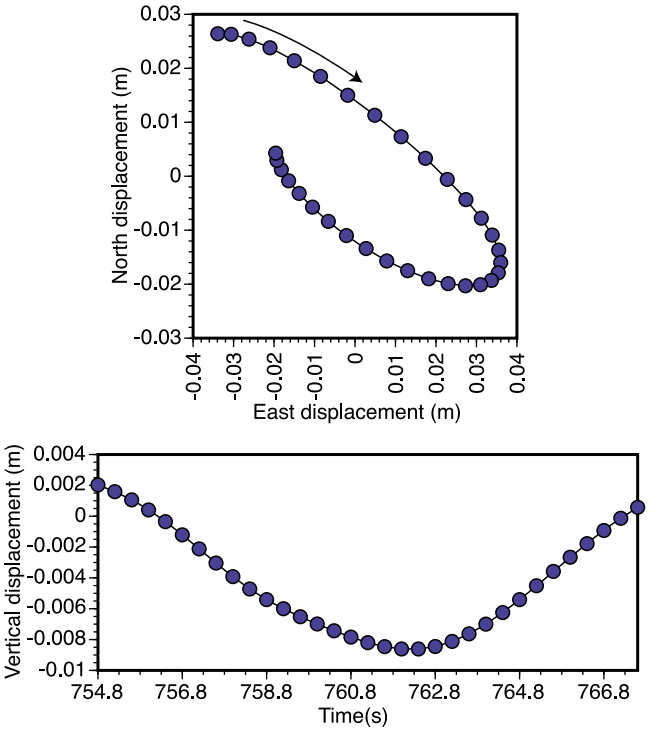

Figure 6. Example particle motions from a single model node representing imposed displacements (loads) on the model. Top panel shows EW-NS motions in map view, and the bottom panel shows vertical displacements. The time scale is the same for both panels. The finite element model enables us to translate these displacements into elastic stress changes.

stress change direction. We interpret unclamping normal stresses as positive, and clamping as negative (Figure 7). Coulomb failure stresses ($\Delta\tau$) can then be calculated as $\Delta\tau \equiv \left|\Delta\bar{\tau}_f\right| + \mu(\Delta\sigma_n - \Delta p)$, where $\Delta\bar{\tau}_f$ is the change in shear stress on the receiver fault (set positive in the direction of fault slip), μ is the coefficient of friction, $\Delta\sigma_n$ is the change in normal stress acting on the target fault (set positive for unclamping), and Δp is pore pressure change (neglected here because of the broad range (μ = 0.2–0.8) of friction coefficient considered).

[15] We calculate a time series of stressing at a point in the center of the model (5 km depth) and plot values of calculated maximum shear, normal, and Coulomb stress for a variety of friction coefficients (Figure 7). We use the plane of maximum shear stress to calculate Coulomb stresses. We note a few general trends from this exercise. Normal stress changes are calculated to be larger than shear stress changes by a factor of approximately 2. This difference is exacerbated by the potential for shear stress changes to be in directions unfavorable for failure. A consequence of normal stress change being larger than shear stress changes is that high friction faults would be expected to see a larger Coulomb stress change (Figure 7), because unclamping has the biggest effect on such faults.

[16] Static stress increases (>0.01 MPa) have been demonstrated to bring faults to failure, with delays ranging from seconds to decades [e.g., *Reasenberg and Simpson*, 1992; *Harris*, 1998; *Stein*, 1999]. We calculate maximum values of dynamic Coulomb stress changes to be up to 4 times greater than this threshold at 0.04 MPa. A key difference though is that while static stress changes are essentially permanent, we calculate the duration of peak dynamic Coulomb stress changes to be less than 6 s (Figure 7).

[17] Our focus has been on identifying maximum stress change. However, to induce an earthquake, the imposed stress changes from seismic waves must line up favorably with the faults that they pass through. Perhaps the simplest way to envision the imposed dynamic stress field is to consider the inclination of the principal stress axes from a vertical reference because these angles can define three primary regimes that favor strike-slip, thrust, and normal faulting. Very generalized regimes can be identified as follows: when both the greatest (σ_1) and least (σ_3) principal stresses lie in, or near the horizontal plane, then strike-slip faulting is favored. If instead σ_1 is

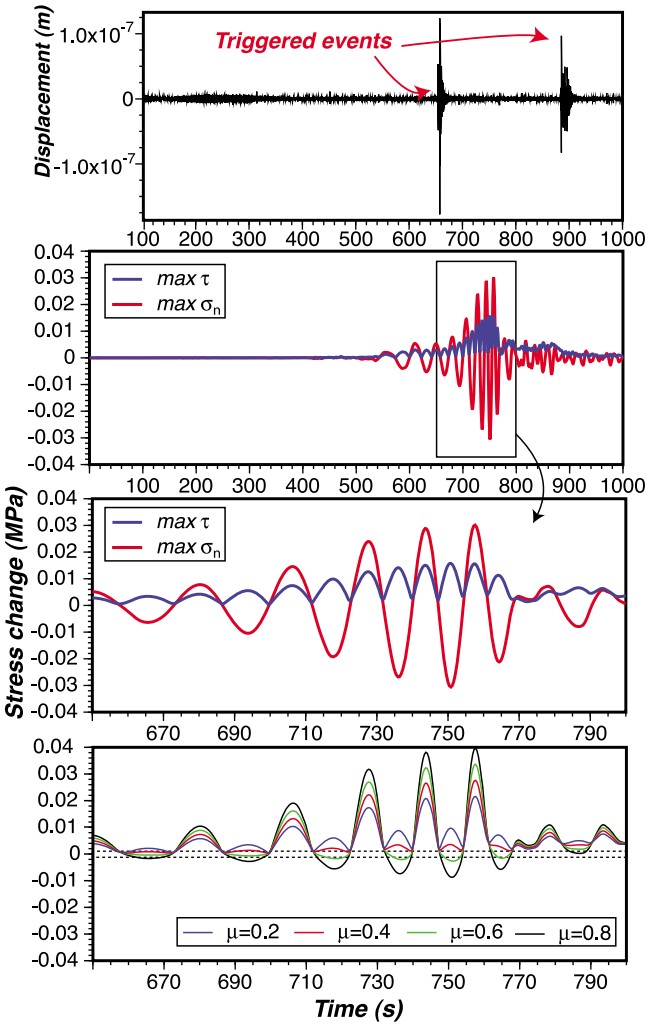

Figure 7. Calculated maximum shear and normal stress changes as derived from principal stress changes for a point at the model center (5 km depth). The uppermost panel shows the timing of small, triggered earthquakes recorded on the Utah Seismograph Network during the passage of surface waves [*Pankow et al.*, 2004]. Maximum shear and normal stress components for the entire 1000 s seismogram, and for a window of maximum stresses are plotted below. The bottom panel shows Coulomb stresses calculated from the shear and normal stress components for a variety of friction coefficients.

near vertical, while σ_3 is horizontal, then normal faulting is favored. Finally, thrust faulting is promoted when σ_1 is horizontal and σ_3 is near vertical.

[18] We note by plotting the inclinations of the principal stress axes of the stress-change tensor that these alignments shift rapidly with time (Figure 8). In the course of 16 s of peak stress change amplitudes, we calculate the stress change regimes passing from favoring strike-slip faulting to normal faulting, then to thrust, back to strike-slip, before flipping to a normal-faulting regime again (Figure 8). Durations of any particular stress-change state last from ~1 to 4 s, and the times that they are also near peak amplitudes are shorter than that, being a fraction of a second.

[19] A focus on the inclination-from-vertical of principal stress axes defines stress regimes; there are further complications resulting from changes in the strike of the most favored failure planes that happen as well. Additionally, imposed stresses can vary with depth on a fault plane. Thus the durations of a given stress regime as shown in Figure 8 are likely maxima for a fault of any given orientation. We explore these effects in detail in the next section.

4. Modeled Fault Slip Triggered by Transient Stresses

[20] An initial step toward understanding the physics of dynamic earthquake triggering is to

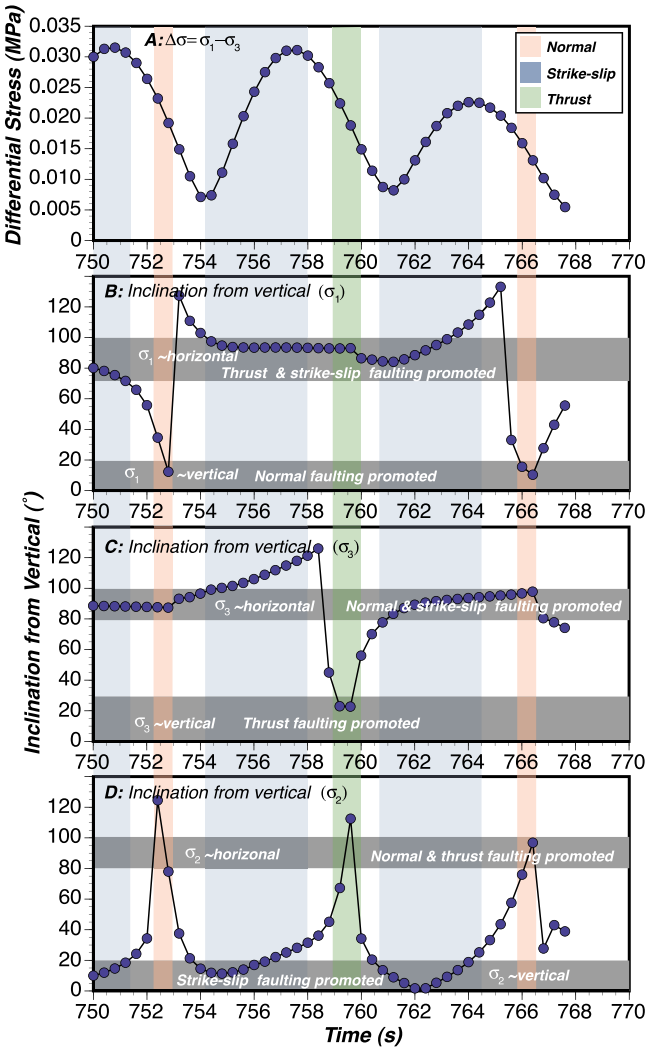

Figure 8. (a) The magnitude of calculated differential stress versus time is shown. Also plotted are inclinations of the principal stresses of the dynamic stress-change tensor as a function of time. (b) σ_1 denotes the greatest principal stress, (c) σ_3 the least principal stress, and (d) σ_2 signifies the intermediate stress. Regimes most favoring thrust, strike-slip, and normal faulting are shaded in green, blue, and red, respectively. Dynamic stress changes rotate rapidly among the different regimes, with durations between ~1 to ~4 s, and much shorter than that at peak amplitudes.

develop a concept about the temporal and spatial evolution of failure stress on a given fault plane. Up to now, we have discussed the calculated time series of dynamic stressing effects at a point. Here we explore dynamic stressing effects on a fault near critical Coulomb failure. We choose a typical normal fault geometry, with a 45° dip that strikes perpendicularly to the azimuth of incoming surface waves that originated from the Denali earthquake; fault dimensions are 15 km long and 10 km wide. This orientation is consistent with observed focal mechanisms of triggered events in Utah [*Pankow et al.*, 2004]. The conceptual failure mechanism involves direct triggering of earthquakes that are otherwise subject to a steady loading rate. The addition of the dynamic stress perturbation would thus move the loading rate further ahead in its cycle. Dynamic stresses are imposed, as calculated from finite element modeling of quasi-dynamic wave propagation in an elastic beam (Figures 4 and 5) to estimate the dynamic stress changes near the Wasatch Front, Utah (Figure 9).

[21] In this modeling case we do not attempt to estimate continuous tectonic loading, but instead simulate failure of a fault just on the cusp of failure. The slip that occurs in the models is therefore only that which can be attributed to dynamic stressing. These failures are therefore small relative to actual tectonic earthquakes, but their rakes and spatial

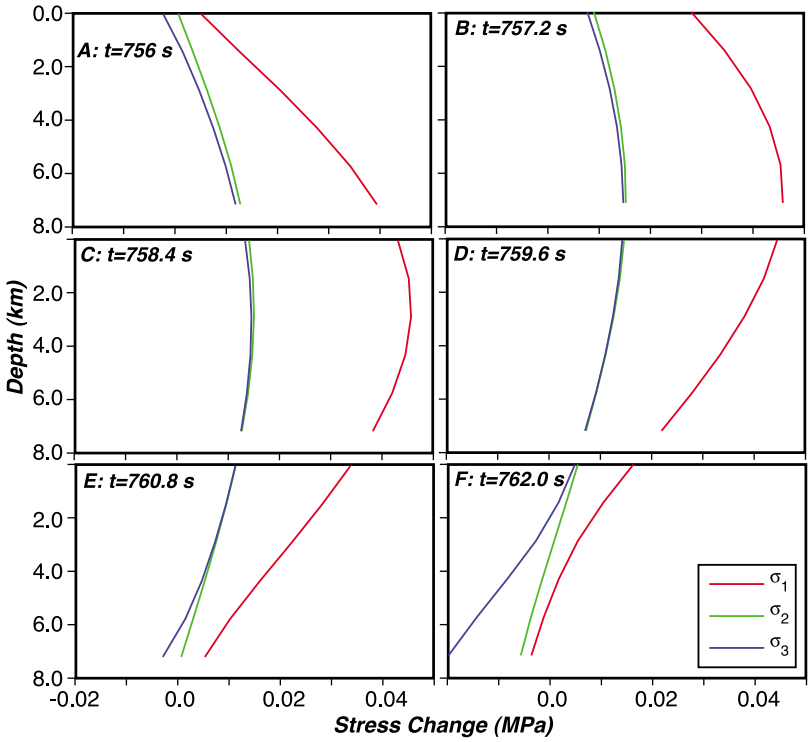

Figure 9. Principal stress change magnitudes are plotted as a function of depth along a 45°-dipping fault surface over time in (a–f) 1.2 s steps.

extent provide insights into the scales and mechanisms of events likely to have been promoted by the Denali surface waves. Failures depicted in Figures 10 and 11 can thus be interpreted as strains during the initial nucleation phase of an eventual triggered earthquake, the full slip distribution in which might evolve to an orientation more in line with the tectonic loading.

[22] Frictional sliding on quasi-statically deforming faults and fractures is modeled using a linear complementarity formulation [*Kaven et al.*, 2012]. This formulation accurately reproduces analytical solutions to static Coulomb friction sliding problems, allows for opening, and does not constrain slip to be parallel to the resolved shear traction. We model slip in response to stress changes in a sequence of 1.2-s time steps across the peak dynamic stress change period by solving for the quasi-static linear elasticity problem with a conservative, constant Coulomb friction ($\mu = 0.6$) along the entire fault surface, which is contained in a linearly elastic, isotropic medium. Friction coefficient choice impacts only the magnitudes of slip (increasing at low coeficients), but not the relative distribution of slip direction, which is the result of interest.

[23] Dynamic stresses for each time step are calculated on the fault surface, which vary with depth as the vertical wavefront encounters the dipping surface (Figure 9). Slip only occurs on the modeled fault at time steps 1 and 6 (corresponds to t = 756 s and t = 762 s in Figures 7 and 8). The other time steps do not reveal any slip because simultaneous contrariant stresses are acting on the plane. At time t = 756, the model fault responds to the passage of dynamic stress by exhibiting shallow strike-slip motion (Figure 10). At the last time step, dip-slip, strike-slip, and opening occur, with left-lateral and opening being the largest relative displacement in response to the passing dynamic stress (Figure 11). Actual opening displacements are not likely to occur on real faults where there is confining pressure, but an opening sense of motion leads to unclamping that can promote triggering by reducing frictional tractions. These transitions in stress-change state can also be seen in Figure 8. While tectonic loading in the Basin and Range favors extensional normal faulting, the passage of the dynamic stresses reveal a different and likely more complicated pattern of promoted slip. We did not attempt to simulate local tectonic loading conditions, so these slip models may not reflect the actual slip that occurred in the Wasatch region. However, the strike-slip predicted by the dynamic stress change may be corroborated by the observations of *Pankow et al.* [2004].

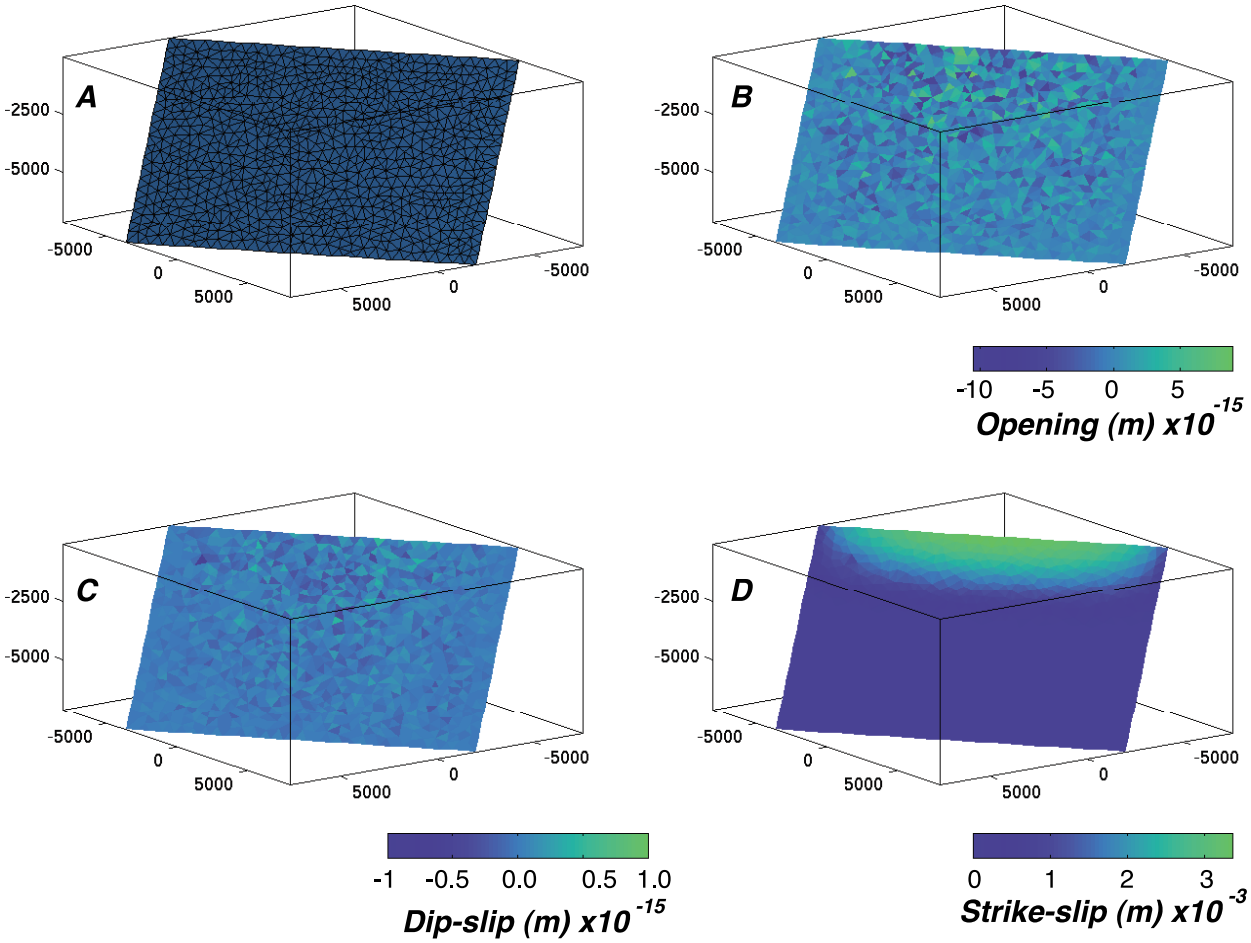

Figure 10. Dynamically triggered failure of a 45°-dipping fault plane oriented orthogonally to surface wave propagation. (a) Fault element meshing is shown. (b) Opening displacements (unclamping positive), (c) dip-slip (downdip is positive), and (d) strike-slip (right-lateral positive) displacements are plotted for t = 756 s. Shallow right-lateral strike-slip failure is the dominant behavior at this time step.

[24] To summarize, the picture of dynamic stressing that emerges from our modeling is one of rapidly varying stresses influencing faults. The sense of slip being promoted can be reversed within a matter of 1–4 s. Faults also have spatially varying stress changes such that only some fraction of the fault area is calculated to slip at any given time. We find that for our 45° dipping test fault, slip does not occur for most of the period where peak stress change conditions are affecting it, potentially consistent with the observed timing of triggered events (Figure 7).

5. Comparison of Model Results With Utah and Other Along-Path Triggered Seismicity Observations

[25] Numerical modeling shows that dynamic stresses are complex and ever-changing. We compare this numerical result with observations by examining western North America earthquakes (source ANSS) for 24-h periods before and after the Denali shock (Figure 12).

[26] A visual examination of where remote triggering happened suggests that the primary areas of rate increase lie in the extensional Basin and Range Province (Figure 12), while the strike-slip regions of California and convergent Pacific Northwest regions appear mostly unchanged. *Pankow et al.* [2004] established that the rate increase in Utah was significant, and *Husker and Brodsky* [2004] found the same result in Idaho and Montana. Both studies identified many triggered earthquakes not reported in the ANSS catalog. It is more problematic to show formal rate increases for the entire western United States region because a uniformly complete catalog has too few events. It is, however, very unlikely that the apparent rate increase can be

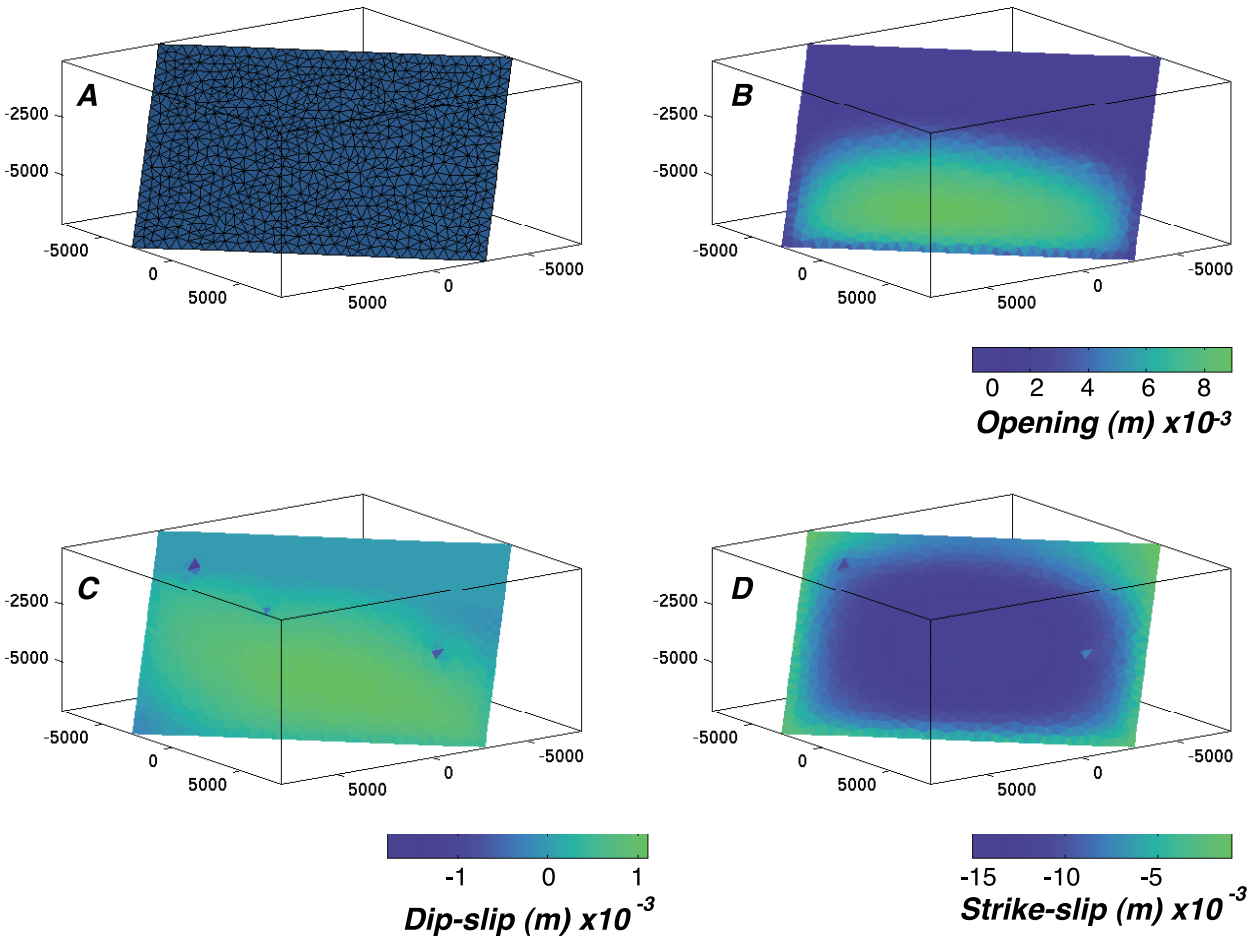

Figure 11. Dynamically triggered failure of a 45°-dipping fault plane oriented orthogonally to surface wave propagation. (a) Fault element meshing is shown. (b) Opening displacements, (c) dip-slip, and (d) strike-slip displacements are plotted for t = 762 s. Simultaneous left-lateral, normal, and unclamping takes place at this time step.

explained by improved detection thresholds during the 24-h period after the Denali event, when they are in fact expected to be diminished [*Kagan*, 2004]. We thus work with the incomplete ±24-h catalog (recognizing the pitfalls in doing so) to qualitatively compare with the numerical modeling predictions.

[27] To establish approximate potential triggered earthquake characteristics, we associate them with the closest faults. The National Seismic Hazards Map Program (NSHMP) provides a database of active faults and, importantly, gives dip information and broad categorization into strike-slip, normal, or thrust designations (source: http://geohazards.usgs.gov/cfusion/hazfaults_search/hf_search_main.cfm). Comparison of nearby faults and earthquake occurrence for the 24-h periods before and after the Denali event yields some interesting features. Most of the events prior to the Denali earthquake were located in the San Andreas Fault system of California (Figure 12a), and thus are associated with faults that have vertical dips (Figure 13a). By contrast, the post-Denali period shows seismicity associated with dominantly 50° dipping faults (Figure 13b). A similar change is noted in fault sense. The number of earthquakes that happened near faults with strike-slip mechanisms stayed roughly the same, whereas we note many more earthquakes in the 24-h period after the Denali earthquake happening near faults classified as normal (Figures 13c and 13d).

[28] Our modeling is consistent with the observation of normal faults being activated, as we calculate that dipping faults would experience unclamping and some normal slip (Figure 11). A puzzling outcome of examining post-Denali seismicity rate changes is that our modeling result indicates strike-slip faulting should also have been promoted, whereas the strike-slip San Andreas system does not show any rate change. Further, we note that thrust faults would also tend to be

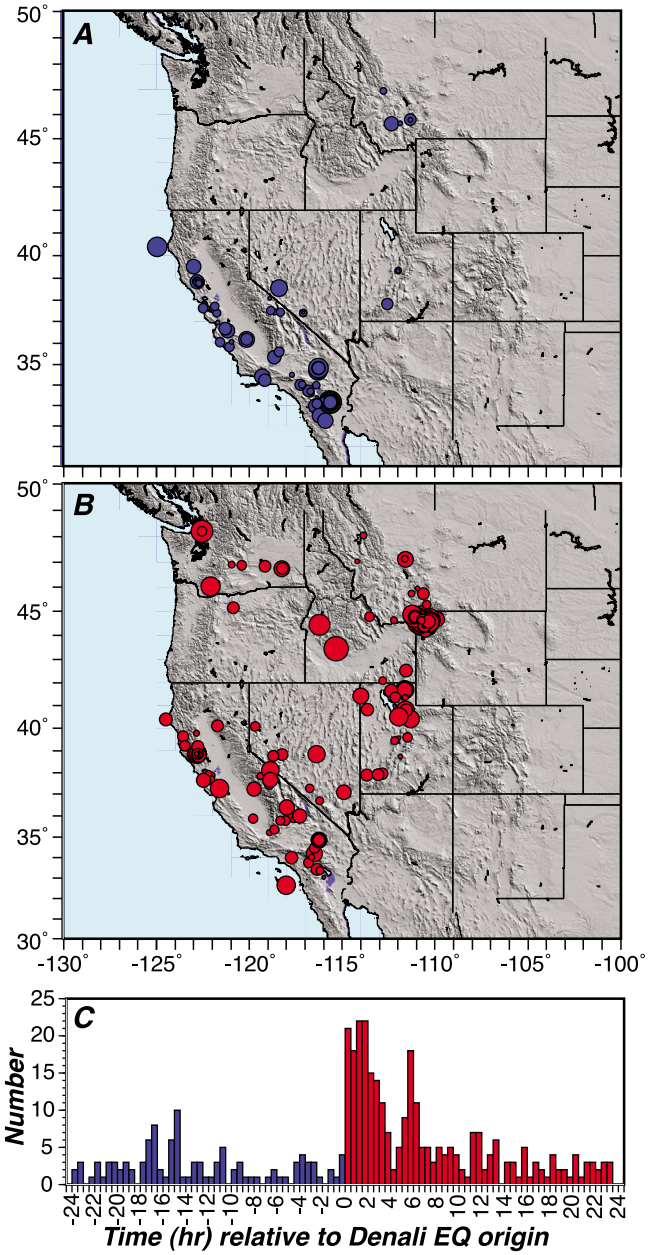

Figure 12. (a) Western United States earthquake occurrence during the 24-h period before the Denali earthquake. Events plotted are for $M \geq 1.0$, so this plot is not asserting a spatially complete catalog. (b) $M \geq 1.0$ earthquake occurrence is plotted for the 24-h period after the Denali event. An obvious rate increase is observed (c) as shown in the histogram, and which was reported by *Gomberg et al.* [2004], *Husker and Brodsky* [2004], and *Pankow et al.* [2004].

encouraged by the dynamic wave train, yet virtually no change in thrust mechanisms are observed (Figure 13) despite the fact that Denali surface waves passed through the convergent Cascadia province on their way to the Basin and Range (Figure 1). This paradox was also noted by *Hill* [2008], and the issue remains unsolved. One insight from our modeling is the tendency for strong periodic unclamping stresses that could conceivably act to depressurize thrust faults that depend on fluid overpressure to slip [*Hubbert and Rubey*, 1959]. Alternatively, *Gomberg et al.* [2004] showed that the spatial patterns of seismicity rate increase after the Denali earthquake were associated with maximum-recorded surface strain. Therefore, rate increases in the Basin and Range Province could be strongly influenced by directivity effects from the Denali earthquake, and triggering may have occurred not only on normal faults, but also on planes of opportunity that could

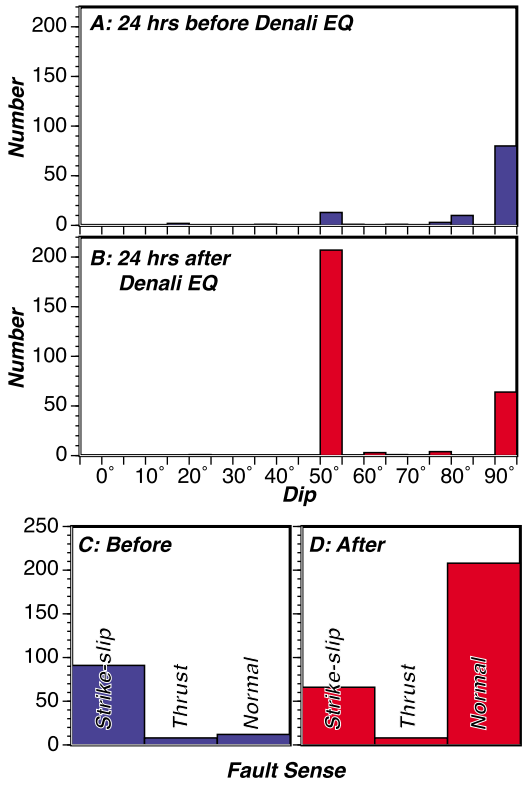

Figure 13. (a) The faults closest to earthquakes that occurred in the 24-h period before the Denali event have primarily vertical dips. (b) The faults closest to earthquakes that occurred in the 24-h period after the Denali event have primarily ~50° dips. The sense of nearest faults differs between the before and after periods with (c) most nearby faults being strike-slip before, and most being (d) normal after.

slip in a strike-slip sense. Detailed observations from the Utah Seismograph Network may be consistent with that conclusion.

[29] *Pankow et al.* [2004] make the following observations: (1) "Double-difference relative relocations for the earthquakes in three of these clusters indicate that most, but not all, of the triggered events were spatially separated from source zones of prior seismicity …." (2) "Focal mechanisms for the two largest triggered events have northeast- to northwest-trending tension axes, which are unusual for the region where they occurred." (3) "The focal mechanism for the M = 3.2 earthquake … shows dominantly strike-slip faulting on a poorly constrained northwest- or northeast-striking plane."

[30] To summarize, observed triggered seismicity in the Basin and Range is not inconsistent with model predictions. However, our calculations predict failure modes that are not observed. Perhaps one explanation for this is that shear stress changes that would drive failure are typically also accompanied by stronger unclamping stresses (Figure 7) that would tend to inhibit thrust faulting. This occurs on our test fault (Figures 10 and 11), which only slips in the normal and strike-slip sense, and experiences significant, but temporary opening displacements.

6. Inferences on Remote Dynamic Triggering: Why are M > 5 Events Rare?

[31] To the extent we can generalize results from modeling the 2002 M = 7.9 Denali earthquake surface waves, we attempt to explain the outcomes from examining global earthquake catalogs that find no associations between $M > 5$ events, while at the same time ubiquitous triggering at lower magnitudes [e.g., *Hill et al.*, 1993; *Brodsky et al.*, 2000; *Kilb et al.*, 2000; *Gomberg et al.*, 2001; *Huc and Main*, 2003; *Gomberg et al.*, 2004; *West et al.*, 2005; *Velasco et al.*, 2008; *Parsons and Velasco*, 2011]. Our models that account for the full wavefield displacement seismograms over time show that dynamic stress changes from surface waves rapidly reverse themselves in the span of a few seconds, and different parts of a fault surface can experience different stress changes simultaneously. Further, the highest amplitudes of dynamic stress change often don't happen at the same times that their directions are aligned with receiver fault rakes. In other words, everything has to line up just right for dynamic triggering to occur. Since there are a lot more small faults than large ones, the odds of a small one lining up are higher.

[32] Surface waves do affect larger faults though, and we note that nucleation of an earthquake in response to dynamic stress changes should be able to occur on such a fault (Figures 10 and 11). However, in our models, the rake of imposed slip often does not match the rake of the target fault (i.e., strike-slip on a normal fault), meaning that it might be difficult for a rupture to spread in the geometrically "wrong" direction. Further, the areas of consistent stress change on a fault are spatially limited, meaning that large-magnitude (hence large rupture area) earthquakes may be more difficult to initiate. Depending on the time necessary for nucleation to spread, it is possible that an incipient earthquake can suddenly be subjected to damping stress changes when the regime is reversed, thus arresting a rupture before it can grow very large. Last, the duration of consistent stress change is

short relative to models of fluid migration times in faults, which may take minutes to hours to respond to imposed normal stress changes [e.g., *Lupi et al.*, 2011]. It is unclear how spatially variable the net change in pore fluid pressure within a fault that is subjected to a time- and space-varying dynamic stress change might be, but these effects could also limit rupture size.

7. Conclusion

[33] Using a 3D finite element model, we model the complete wavefield from the 2002 M = 7.9 Denali earthquake recorded near the Wasatch Front in Utah. We find that the stress-change regime varies rapidly between favoring strike-slip, thrust, and normal faulting, with durations lasting ∼1–4 s and that these stress regimes usually affect only some fraction of a fault surface at any given time. Stress amplitudes also vary, suggesting that ideal conditions for triggering are short-lived and spatially limited. Given these stressing conditions, our modeling indicates that it may be difficult for a larger rupture area to experience the temporally and spatially coherent stress change necessary to develop into a large magnitude earthquake. In conclusion, while we have no basis to say that a large, remotely triggered earthquake cannot happen, our models of dynamic stressing point to reasons why such events should be rare.

Acknowledgments

[34] We thank two anonymous reviewers and Editor Thorsten Becker for constructive and helpful comments on this paper. We also appreciate the use of the Generic Mapping Tools (GMT) program [*Wessel and Smith*, 1991].

References

Belardinelli, M. E., A. Bizzarri, and M. Coco (2003), Earthquake triggering by static and dynamic stress changes, *J. Geophys. Res.*, *108*(B3), 2135, doi:10.1029/2002JB001779.

Birch, F. (1966), Compressibility; elastic constants, *Mem. Geol. Soc. Am.*, *97*, 97–173.

Brodsky, E. E., and S. G. Prejean (2005), New constraints on mechanisms of remotely triggered seismicity at Long Valley Caldera, *J. Geophys. Res.*, *110*, B04302, doi:10.1029/2004JB003211.

Brodsky, E. E., V. Karakostas, and H. Kanamori (2000), A new observation of dynamically triggered regional seismicity: Earthquakes in Greece following the August, 1999 Izmit, Turkey Earthquake, *Geophys. Res. Lett.*, *27*, 2741–2744, doi:10.1029/2000GL011534.

Brodsky, E. E., E. Roeloffs, D. Woodcock, I. Gall, and M. Manga (2003), A mechanism for sustained groundwater pressure changes induced by distant earthquakes, *J. Geophys. Res.*, *108*(B8), 2390, doi:10.1029/2002JB002321.

Capozza, R., A. Vanossi, A. Vezzani, and S. Zapperi (2009), Suppression of friction by mechanical vibrations, *Phys. Rev. Lett.*, *103*, 085502, doi:10.1103/PhysRevLett.103.085502.

Gomberg, J., M. L. Blanpied, and N. M. Beeler (1997), Transient triggering of near and distant earthquakes, *Bull. Seismol. Soc. Am.*, *87*, 294–309.

Gomberg, J., N. M. Beeler, M. L. Blanpied, and P. Bodin (1998), Earthquake triggering by transient and static deformation, *J. Geophys. Res.*, *103*, 24,411–24,426, doi:10.1029/98JB01125.

Gomberg, J., P. Reasenberg, P. Bodin, and R. Harris (2001), Earthquake triggering by transient seismic waves following the Landers and Hector Mine, California earthquakes, *Nature*, *411*, 462–466, doi:10.1038/35078053.

Gomberg, J., P. Bodin, K. Larson, and H. Dragert (2004), Earthquake nucleation by transient deformations caused by the M = 7.9 Denali, Alaska, earthquake, *Nature*, *427*, 621–624, doi:10.1038/nature02335.

Gonzalez-Huizar, H., and A. A. Velasco (2011), Dynamic triggering: Stress modeling and a case study, *J. Geophys. Res.*, *116*, B02304, doi:10.1029/2009JB007000.

Harris, R. A. (1998), Introduction to special section: Stress triggers, stress shadows, and implications for seismic hazard, *J. Geophys. Res.*, *103*, 24,347–24,358.

Hill, D. P. (2008), Dynamic stresses, Coulomb failure, and remote triggering, *Bull. Seismol. Soc. Am.*, *98*, 66–92, doi:10.1785/0120070049.

Hill, D., and S. Prejean (2007). Dynamic triggering, in *Treatise on Geophysics*, vol.4, *Earthquake Seismology*, edited by H. Kanamori, pp. 293–320, Elsevier, Amsterdam, Netherlands.

Hill, D. P., et al. (1993), Seismicity in the western United States remotely triggered by the M 7.4 Landers, California, earthquake of June 28, 1992, *Science*, *260*, 1617–1623, doi:10.1126/science.260.5114.1617.

Hubbert, M. K., and W. W. Rubey (1959), Role of fluid pressure in mechanics of overthrust faulting, *Geol. Soc. Am. Bull.*, *70*, 115–166, doi:10.1130/0016-7606(1959)70[115:ROFPIM]2.0.CO;2.

Huc, M., and I. G. Main (2003), Anomalous stress diffusion in earthquake triggering: Correlation length, time dependence, and directionality, *J. Geophys. Res.*, *108*(B7), 2324, doi:10.1029/2001JB001645.

Husker, A. L., and E. E. Brodsky (2004), Seismicity in Idaho and Montana triggered by the Denali fault earthquake: A window into the geologic context for seismic triggering, *Bull. Seismol. Soc. Am.*, *94*, S310–S316, doi:10.1785/0120040618.

Iwata, T. (2008), Low detection capability of global earthquakes after the occurrence of large earthquakes: Investigation of the Harvard CMT catalogue, *Geophys. J. Int.*, *174*, 849–856, doi:10.1111/j.1365-246X.2008.03864.x.

Kagan, Y. Y. (2004), Short-term properties of earthquake catalogs and models of earthquake source, *Bull. Seismol. Soc. Am.*, *94*, 1207–1228, doi:10.1785/012003098.

Kaven, J. O., S. H. Hickman, N. C. Davatzes, and O. Mutlu (2012), Linear complementarity formulation for 3D frictional sliding problems, *Comput. Geosci.*, *16*, 613–624, doi:10.1007/s10596-011-9272-0.

Kilb, D. (2003), A strong correlation between induced peak dynamic Coulomb stress change from the 1992 *M*7.3 Landers, California, earthquake and the hypocenter of the 1999 *M*7.1 Hector Mine, California, earthquake, *J. Geophys. Res.*, *108*(B1), 2012, doi:10.1029/2001JB000678.

Kilb, D., J. Gomberg, and P. Bodin (2000), Triggering of earthquake aftershocks by dynamic stresses, *Nature*, *408*, 570–574, doi:10.1038/35046046.

Kilb, D., J. Gomberg, and P. Bodin (2002), Aftershock triggering by complete Coulomb stress changes, *J. Geophys. Res.*, *107*(B4), 2060, doi:10.1029/2001JB000202.

Lupi, M., S. Geiger, and C. M. Graham (2011), Numerical simulations of seismicity-induced fluid flow in the Tjörnes Fracture Zone, Iceland,, *J. Geophys. Res.*, *116*, B07101, doi:10.1029/2010JB007732.

Oye, V., and W. Ellsworth (2007), Monitoring microearthquakes with the San Andreas Fault Observatory at depth, in *SPE - 69th European Association of Geoscientists and Engineers Conference and Exhibition 2007*, vol. 2, pp. 747–751, Eur. Assoc. of Geosci. and Eng., Houten, Netherlands.

Pankow, K. L., W. J. Arabasz, J. C. Pechmann, and S. J. Nava (2004), Triggered seismicity in Utah from the 3 November 2002 Denali Fault Earthquake, *Bull. Seismol. Soc. Am.*, *94*, S332–S347, doi:10.1785/0120040609.

Parsons, T. (2005), A hypothesis for delayed dynamic earthquake triggering, *Geophys. Res. Lett.*, *32*, L04302, doi:10.1029/2004GL021811.

Parsons, T., and A. A. Velasco (2011), Absence of remotely triggered large earthquakes beyond the main shock region, *Nat. Geosci.*, *4*, 312–316, doi:10.1038/ngeo1110.

Reasenberg, P. A., and R. W. Simpson (1992), Response of regional seismicity to the static stress change produced by the Loma Prieta earthquake, *Science*, *255*(5052), 1687–1690.

Roy, M., and C. Marone (1996), Earthquake nucleation on model faults with rate- and state-dependent friction: Effects of inertia, *J. Geophys. Res.*, *101*(B6), 13,919–13,932, doi:10.1029/96JB00529.

Scholz, C. H. (1998), Earthquakes and friction laws, *Nature*, *391*, 37–42, doi:10.1038/34097.

Stein, R. S. (1999), The role of stress transfer in earthquake occurrence, *Nature*, *402*, 605–609, doi:10.1038/45144.

Sturtevant, B., H. Kanamori, and E. E. Brodsky (1996), Seismic triggering by rectified diffusion in geothermal systems, *J. Geophys. Res.*, *101*, 25,269–25,282, doi:10.1029/96JB02654.

Velasco, A. A., S. Hernandez, T. Parsons, and K. Pankow (2008), The ubiquitous nature of dynamic triggering, *Nat. Geosci.*, *1*, 375–379, doi:10.1038/ngeo204.

Vincenty, T. (1975), Direct and inverse solutions of geodesics on the ellipsoid with application of nested equations, *Surv. Rev. XXII*, *176*, 88–93.

Wessel, P., and W. Smith (1991), Free software helps map and display data, *Eos Trans. AGU*, *72*(441), 445–446.

West, M., J. J. Sanchez, and S. R. McNutt (2005), Periodically triggered seismicity at Mount Wrangell, Alaska, after the Sumatra earthquake, *Science*, *308*, 1144–1146, doi:10.1126/science.1112462.